High-order simulation of a rotor in forward flight using a four-dimensional adaptive flow solver

H. van der Ven and O.J. Boelens

Flight Physics and Loads Department
National Aerospace Laboratory
P.O.Box 90502
1006 BM Amsterdam
The Netherlands
venvd@nlr.nl, boelens@nlr.nl

Abstract The accurate simulation of the rotor wake using first-principles based CFD is primarily a gridding problem. In order to capture the tip vortices the computational mesh must be refined in the vortex regions, which are not known beforehand and change position over time. In this paper, a high-order Discontinuous Galerkin method is combined with a pre-adaptation scheme on four-dimensional space-time meshes. An iterative pre-adaptation scheme is proposed, where the mesh is first refined on blade tip trajectories, and subsequently on streak lines of particles released at the blade tip. The streak lines are computed based on the flow solution obtained on the previous mesh. The algorithm is applied to the isolated 7AD1 rotor in high-speed flight. Comparison with experiment is favourable. The effectiveness of the pre-adaptation strategy combined with high-order simulation is demonstrated.

1 Introduction

In level helicopter flight there are two regimes with high vibration levels, low speed transition flight and high speed forward flight. The two high vibration regimes translate directly into high operating and maintenance costs (Datta et al. [2]). There are three key aerodynamic phenomena which contribute to the vibratory loads: wake induced airloads, compressibility effects, and dynamic stall. The current paper is focused on the accurate resolution of wake-induced airloads using Computational Fluid Dynamics (CFD) techniques.

As summarised by Datta et al. [2], first principles CFD calculation of the wake is primarily a grid refinement problem. In order to capture the tip vortices the computational mesh must be refined in the vortex regions, which are not known beforehand. The dynamic nature of the wake in forward flight complicates the refinement problem since the vortices change position over time.

In recent years, the Netherlands National Aerospace Laboratory NLR has developed the four-dimensional MTMG algorithm for accurate rotor simulation. The algorithm is especially designed for those flight conditions where the detailed resolution of the wake is of the utmost importance [15], [6], [14]. The main design principle is to attain efficiency in the number of degrees of freedom, while maintaining a scalable algorithm on parallel machines. The aerodynamic CFD module in the algorithm demonstrates good vortex capturing capabilities, using local mesh refinement in both space and time, for relatively short turnaround times. A drawback of the method is its high memory requirement. For the simulation of a BO105 in BVI conditions it turns out that the resolution required to track the tip vortex for one and a half rotor revolution was unattainable using NLR's computing resources.

High order methods in principle have the capability of resolving the vortex with less degrees of freedom than conventional schemes. Hariharan and Sankar [4] have demonstrated that a 7^{th} order ENO scheme is capable of capturing the tip vortex over 1-2 revolutions using only five points across the vortex core. The drawback of an ENO scheme is its non-local character, making it difficult to combine with a local mesh refinement algorithm. Discontinuous Galerkin (DG) methods [1] do not have that drawback: in principle, arbitrarily high-order schemes can be constructed on locally refined meshes with hanging nodes.

In this paper the higher-order DG method is applied to the simulation of a trimmed isolated rotor with elastic blades in high-speed flight. The outline of the paper is as follows: in the next section the numerical method is briefly

described. In Section 3 the high-speed test case is described. Section 4 describes the grid adaptation strategy for shocks and vortex wake, illustrated by the actual grid used in the simulation. Flow simulation results are presented in Section 5. Finally, in Section 6 conclusions are drawn.

2 Numerial method

The numerical method is a high-order DG scheme combined with an efficient space-time solver MTMG for time-periodic problems.

2.1 *Multi-time multi-grid algorithm*

The basic idea of the multi-time multi-grid (MTMG) [15] algorithm is that a time-periodic problem can be considered a steady problem in the sense that after one time period the next period shows the same physical phenomena. This is formalised by solving the time-dependent equations simultaneously in both space and time for the complete period of the problem. This is contrary to the usual time-serial approach, where one proceeds time step after time step on spatial grids. Now the time-dependent equations are solved on a four-dimensional space-time grid which contains all time levels in a period. Apart from generating a periodic solution by construction, the most relevant advantage for rotor simulations is that the time-accurate coupling of different physics models is straightforward. Another important benefit is that local grid refinement can be applied in space and time, while maintaining a scalable algorithm on massively parallel machines.

The current algorithm contains four modules, an aerodynamic module for the solution of the flow equations, a mesh refinement module to improve vortex resolution in the flow domain, an elastic module to account for the elastic blade deformations, and a trim module to trim the rotor system.

2.2 *Discontinuous Galerkin finite element method*

The compressible Euler equations of gas dynamics are solved using the discontinuous Galerkin (DG) finite element method in an arbitrary Lagrangian-Eulerian formulation to accommodate moving meshes. Details of the flow solver can be found in Van der Vegt et al. [10]. Of particular relevance for the simulation of vortex flow is the fact that the DG method not only solves for cell-averaged flow data, but also for the flow gradients. The flow gradients are used to determine the vorticity directly and as such vorticity transport is contained in the discrete equations. Moreover, the DG method is ideally suited for local grid refinement.

The flow gradients are part of the numerical scheme by combining constant basis functions within each element with linear basis functions. An obvious extension to the scheme is to allow quadratic or cubic basis functions. This effectively increases the order of accuracy of the scheme to three or four. The drawback is that the number of degrees of freedom per element is also increased. In one dimension, the second order scheme has two degrees of freedom per element, the third order scheme has three, and the fourth order scheme has four. In higher dimensions, the increase in the number of degrees of freedom is more dramatic: the second order scheme in four dimensions has five degrees of freedom per element, third order 15, and fourth order 35. In this paper, the third order scheme will be applied, and compared with the second order scheme.

As shown above, the third order scheme solves three times as many unknowns as the second order scheme. For the stepping-stone test case of 2D vortex convection it has been found that the third order method has the same resolution characteristics as the second order method on a mesh which is once refined in every direction. For four-dimensional simulations such a uniformly refined mesh contains 16 times more grid points, so it is expected that the third order scheme is 16/3 times more efficient than the second order scheme.

3 Test case

Data point 135 of the Helishape wind tunnel program is simulated [10]. This data point concerns a high-speed level flight case at an advance ratio of 0.356 for the isolated 7AD1 rotor with parabolic and anhedral tip. The blade has a radius R of 2.1m and a chord c of 0.14m (aspect ratio R/c=15).

The flow displays (weak) shocks at the advancing side and the vortex wake contributes

to the vibratory loads at the rotor hub. Hence a CFD mesh must be generated capable of resolving shocks and vortices.

4 Adaptation strategy

For industrial applications the most common grid adaptation strategy is to use sensors based on flow features. Shock sensors based on gradients in the flow have in general been quite effective in resolving shocks. For tip vortices in the rotor wake the effectiveness of feature-based sensors is not so clear. The straightforward vorticity magnitude sensor does not discriminate between tip vortices, vortex sheets or numerically induced boundary layers. More advanced sensors, such as the λ_2 criterion (Jeong et al. [6]), require significant resolution of the vortex to detect it. Such a resolution is not present on the initial coarse meshes. Because of these findings, it was concluded to opt for pre-adaptation, where the mesh is refined before the actual flow computation, based on the expected location of the tip vortices. This will be explained in detail later. In effect, the pre-adaptation strategy resembles unstructured grid generation more than conventional mesh refinement. It is comparable to the Chimera approach of Dietz et al. [4], where Chimera grids are constructed around the expected tip vortex locations. The benefit of our approach is that it is still based on the single-grid concept.

4.1 *Relevant scales*

Since we solve the Euler equations there is no physical limit to the vortex strength. Under mesh refinement the tip vortices will grow stronger and stronger. In order to avoid excessive grid refinement, the cell diameters should be limited from below. The minimal cell diameter is in general set to $R/200$, which is one quart of the experimentally determined vortex core size, where R is the rotor radius (Caradonna, [2]). Roughly speaking, this resolution corresponds to 12 degrees of freedom in each direction in the vortex core for the third-order DG method.

In order to avoid dispersion of the vortex in time, the physical time step in the vortex should correspond to a CFL number $u\Delta t/\Delta x$ of the order of one. The reference velocity is the magnitude of the freestream velocity. Note that we have taken the CFL number corresponding to the convective velocity and not the acoustic signals, since the main mechanism in the wake is convection of vorticity. Let T be the period of one revolution, then the time step restriction translates to the following relation:

$$\frac{\Delta t}{T}=\frac{\Delta x}{uT}=\frac{\Delta x}{2\pi R}\frac{\Omega R}{u}=\frac{\Delta x/R}{2\pi\mu},$$

where μ is the advance ratio. With $\Delta x/R = 1/200$, an advance ratio of 0.35 we need about four hundred time steps for one revolution, or one hundred for one period of a four-bladed rotor, corresponding to an increment of less than one degree azimuth. Note that this time step should be sufficient for the convection of the vortex, but not necessarily for blade-vortex interaction.

4.2 *Pre-adaptation on blade geometry*

For the four-dimensional algorithm it is of the utmost importance to be efficient in the number of grid points. Using the pre-adaptation strategy as a kind of grid generation, the starting grid should be as coarse as possible. At NLR, the starting grid is generated using a multi-block structured grid generator. In a block-structured grid, the resolution required at the geometry will extend into the flow domain. In order to reduce the number of elements, a coarse mesh is generated, which is subsequently locally refined near the blades. Care is taken that the blade geometry is well-represented under local refinement. An impression of the resolution of the resulting mesh is shown in Figure 1. The number of elements is 64 in the chord direction and 104 in the span direction.

The space-time mesh obtained using this geometry refinement is referred to as Mesh G0. It contains 12.3 million elements, distributed over 64 time levels, which is close to the 100 time levels required for vortex convection. The blade motion has been trimmed on this mesh, taking into account elastic blade deformations.

4.3 *Pre-adaptation on blade tip trajectories*

By their nature, the location of the tip vortices is predominantly determined by the trajectory of the tip. So, to a very good approximation, the vortex trajectories can be taken to be the blade

tip trajectories. The blade tip trajectories $\Gamma(t)$ at time t are cycloids, described by

$$\Gamma(t) = \{ (R\cos(\Omega(t-s)), R\sin(\Omega(t-s)), w(t-s)) + \vec{u}_\infty s \mid s \geq 0 \},$$

where Ω is the rotor frequency, $w=w(t)$ is the flapping motion of the tip, and $\vec{u}_\infty$ is the free stream velocity.

Based on this geometrical information, the mesh may be pre-adapted to increase the resolution near the tip trajectories. Whenever a cell is within a given distance of a tip trajectory and the mesh width or the time step is greater than a given threshold the cell is refined. Eventually a mesh is 'generated' with uniform space-time resolution in the expected vortex regions. The main benefit of this method is that there will be no refinement in other regions, for instance in the vortex sheets, hence the total number of grid cells is reduced compared to feature-based adaptation.

4.4 *Pre-adaptation on streak lines*

Of course, the assumption that the tip vortices follow the tip trajectories ignores the effects of downwash, contraction and interaction. This can be remedied by increasing the area around the trajectories which will be refined, but this will significantly increase the number of grid cells. Another option would be to replace the free stream velocity in the definition of the tip trajectories $\Gamma(t)$ by the computed velocity field, that is, determine the streak lines of particles released at the blade tip.

In this way, an iterative pre-adaptive procedure is constructed, where the accuracy of the predicted tip vortex locations is increased with each iteration. In Figure 3 and Figure 4, a comparison is made between the blade tip trajectories and the streak lines of particles released at the blade tips (using the flow results of the next section). The difference increases with the age of the vortex. The main difference between the two methods is that the second accounts for the downwash of the rotor.

Three adaptations have been carried out, resulting in the following grids:

G1. Adaptation on blade tip trajectories, with a target mesh width of 0.0075R within a distance of 0.05R of the trajectories. The mesh contains 14.3 million elements.

G2. Adaptation based on streak lines using the flow solution on Mesh G1, with a target mesh width of $0.0075R=0.11c$ at a distance of $0.0375R$ of the streak lines. The mesh contains 15.4 million elements.

G3. As G2, but the target mesh width is $0.005R=0.075c$. The mesh contains 19.3 million elements.

The 19.3 million elements of Mesh G3 are equivalent to 290 million degrees of freedom per equation. Since the space-time mesh contains 64 time slabs, the average number of degrees of freedom per time slab is 4.5 million. This clearly is a modest number when trying to resolve the rotor wake.

It should be remarked that the target mesh width is not necessarily attained. A cell is refined whenever the mesh width is more than two times the target mesh width. Hence, on the final mesh, mesh widths will be between once and twice the target mesh width. Moreover, out of practical considerations, the mesh adaptation is stopped before saturation of the refinement criterion, and the quality of the mesh is judged by inspection.

Figure 5 and Figure 6 show Mesh G3 at two horizontal cross sections. The expected tip vortex locations are shown as curves, and blanked when the distance of the curve to the plane is greater than $0.0375R$, which is the user-defined distance within which cells should be refined.

Figure 7 up to Figure 9 illustrate the pre-adaptation algorithm for the three meshes in a grid plane through the rotor axis and approximately perpendicular to the vortices. For Mesh G2 the attained resolution in the expected vortex regions is about $0.01R=0.15c$. For Mesh G3 the attained resolution is about $0.006R=0.09c$.

It is clear from these figures that the mesh has been refined in a uniform way near the predicted vortex locations, and nowhere else. Hence the pre-adaptation algorithm is very effective in limiting the number of refined elements.

5 Flow results

In the experiment the rotor is trimmed for thrust, drag and zero flapping. The latter is not possible in our MTMG framework, so the rotor is trimmed for thrust and zero pitching and rolling moment. Once trimmed, the flapping motion was seen to be small: at most one degree at the retreating side. Hence it is expected that at the advancing side the flow conditions in the simulation are comparable to those of the experiment.

Once the rotor is trimmed, the resolution near the blades on the advancing side has been improved using the standard shock sensor. An illustration of the resulting mesh is shown in Figure 2. Next, the pre-adaptation strategy is applied, and the Meshes G1 up to G3 have been generated. Please note that the locally refined meshes still contain the trimmed and elastic blade motion.

Pressure distributions at selected stations and azimuth angles are compared with experimental data in Figure 10. Simulation results are obtained on Mesh G3. General agreement is good. As expected, the pressure distributions at the retreating side ((c) and (h)) show greater differences, probably due to the differences in blade motion because of different trimming procedures. Agreement at the advancing side at 92% blade is very good, the agreement at 82% and 70% blade is satisfactory. It is expected that the relatively coarse resolution of the near blade mesh is the cause of this. The mesh at 92% blade has been locally refined using the shock sensor (see Figure 2), whereas at the more inboard stations the resolution is that of the Mesh G0 (see Figure 1).

Time histories of the pressure at selected blade stations are shown in Figure 11. Simulation results are obtained on Mesh G3. Overall agreement with experiment is evident. Of special interest are the stations near the leading edge at the lower side of the blade, which are the most sensitive to vortex interaction. The vortex interaction is visible at the lower side at all span stations for x/c=0.06. The amplitude is underpredicted for r/R=0.7, but in quite good agreement for the other two stations. At span station r/R=0.82 the simulation shows the same two peaks as the experiment, albeit at different amplitudes and a phase shift of -20 degrees azimuth. The same phase shift is visible at span station r/R=0.92, but the simulation reproduces much of the frequency content of the experiment. The reader is referred to Steijl et al. [10] for a detailed discussion on phase shifts in high-speed flight. Based on their findings, the phase shift in the current simulation is most probably caused by the different blade motion, since the trim of the simulation differs from the experimental trim.

The effect of discretization scheme and resolution at the span station r/R=0.82 is shown in detail in Figure 12. The second-order simulation on the mesh without vortex refinement shows the correct trend, but misses the vortex interaction. The second-order simulation on the Mesh G2 does show the first interaction, bur misses the second, whereas the third-order simulation on Mesh G2 captures both interactions.

Figure 13 compares the time histories at the span stations r/R=0.82 and r/R=0.92 for Mesh G2 and Mesh G3, in order to assess the importance of the mesh resolution for the resolution of the vortex interactions. The interaction at r/R=0.82 is already visible on Mesh G2. The interaction at r/R=0.92 is completely missed on Mesh G2. On Mesh G2 the tip vortex of the preceding blade is too weak to interact with the blade pressures.

Figure 14 shows the vortex systems at an azimuth angle of 56 degrees, for second and third order solutions on Mesh G2 and G3. Clearly, the second order simulations show little evidence of vortices at the shown vorticity levels: the vortices are present but weak. The third order solutions show much improvement over the second order solutions. The increased resolution on Mesh G3 results in stronger vortices which persist longer.

Figure 15 displays the vortex system, viewed from below, at an azimuth angle of 56 degrees as computed on Mesh G3. Since the vortex wake is located below the rotor disk, this view presents a clear picture of the vortex system. Vortices 1 and 2 (numbering as in the figure) are clear and concentrated. Vortex 3 is less concentrated: it is slightly weaker than the previous vortices, and the iso-contour is no longer fully contained in the refined and uniform vortex region, causing a ragged

representation of the iso-contour. Of interest is the interaction of Vortex 3 with the wake of the root vortex (near the 'x' in the figure). The interaction causes the vortex to break. Whether this is a physical phenomenon or is a consequence of the hub modelling is an open issue.

In order to assess the accuracy of the streak lines pre-adaptation strategy the locations of the tip vortices in Mesh G3 are compared with the refinement locations in Figure 16 up to Figure 23. The vortices shown and numbered in Figure 18, from left to right, are 1) the tip vortex of the preceding blade (now at ψ=208^o), 2) tip vortex of the blade before the preceding blade (now at ψ=298^o), 3) the vortex sheet and root vortex of the preceding blade (now at ψ=208^o), 4) the root vortex of the next blade (now at ψ=298^o), 5) some debris from the root vortices, 6) the tip vortex of the blade which is now at ψ=28^o. Comparing the two vortex systems, the strength of vortex (2) has clearly improved, and the vortex is located at the exact position where the mesh has been refined. The next two refinement area's, designated for the older tip vortices, fail to resolve any vorticity. This is most probably caused by the interaction with the root vortices, which have stronger interactional effects than the wake of a hub would have.

In Figure 22 the vortex locations and pre-adaptation regions are compared for a slice which does not intersect the rotor centre, so the effect of the hub modelling should be less devastating. Again, vortex (2) in downstream direction is much stronger on Mesh G3 than on Mesh G2. On Mesh G3 vortex (3) is gaining in strength, but hardly visible on Mesh G2. All three vortices are located within the refinement regions (see Figure 23), demonstrating the accuracy of the pre-adaptation algorithm.

The pre-adaptation algorithm is an iterative algorithm in the sense that each flow solution on a given refined mesh will in principle produce different streak lines than the streak lines used for the refinement. Figure 24 and Figure 25 compare the streak lines obtained from the flow solutions on Mesh G2 and G3. Differences are small compared to the radius of 0.0375*R* (the distance below which elements are refined). Hence it can be concluded that the iterative process of grid refinement on streak lines converges.

Figure 26 compares the streak lines on Mesh G3 with the vortex locations on the same mesh. Within the tolerance of 0.0375*R* the streak lines coincide with the vortex centres. Hence, the streak lines of particles released from the blade tips provide a sufficiently accurate prediction of the tip vortex locations.

This section is concluded with a discussion on the computational complexity of the algorithm. The trim is executed on the coarse mesh without vortex refinement, and is negligible compared to obtaining the third-order solution on the vortex-refined mesh. Pre-adaptation takes about one day, to obtain the flow solution takes four and a half days at four processors of the NEC SX-8R at 23 Gflop/s sustained. Memory requirement for the third-order simulation on the mesh with 19 million elements is 87GB. Note that at a peak speed of 128 Gflop/s the NEC SX-8R/8 is a small compute server. Considering the scalability of the algorithm, the simulations described in this paper are expected to take less than a day on a teraflop machine.

6 Conclusions

A comprehensive approach to the simulation of the rotor wake using first-principles CFD has been presented. The effectiveness of the pre-adaptation strategy for the vortex-convection for an isolated rotor in high-speed flight has been demonstrated. Agreement with experiment is relatively good.

Acknowledgements

The work described in this paper is partially funded by the EU 6FP 'ADIGMA' project under Contract No. AST5-CT-2006-030719, and partially by NLR's programmatic research.

References

[1] O.J. Boelens, H. van der Ven, B. Oskam, and A.A. Hassan. Boundary conforming discontinuous Galerkin finite element approach for rotorcraft simulations. *J. of Aircraft*, **39** (5):776–785, sep-oct 2002.

[2] F.X. Caradonna, Development and challenges in rotorcraft aerodynamics, AIAA-2000-0109, 2000.

[3] A. Datta, M. Nixon, and I. Chopra. Review of rotor loads prediction with the emergence of rotorcraft CFD. *J. American Helicopter Society*, **52**(4): 287-317, 2007.

[4] M. Dietz, E. Kramer, and S. Wagner, Tip vortex conservation using on a main rotor in slow descent flight using vortex-adapted Chimera grids, AIAA-2006-3478, 2006.

[5] N. Hariharan and L.N. Sankar. High-order essentially nonoscillatory schemes for rotary-wing wake computations. *J. of Aircraft*, **41**(2): 258-267, 2004.

[6] J. Jeong and F. Hussain, On the identification of a vortex, *J. Fluid Mech.*, **285**, 69-94, 1995.

[7] Norbert Kroll, ADIGMA – A European project on the development of adaptive higher order variational methods for aerospace applications, ECCOMAS CFD 2006, Egmond aan Zee, 2006.

[8] J. W. Lim, R. C. Strawn, Prediction of HART II rotor BVI loading and wake system using CFD/CSD loose coupling, AIAA paper 2007-1281.

[9] Mark Potsdam, Hyeonsoo Yeo, and Wayne Johnson, Rotor Airloads Prediction Using Loose Aerodynamic/Structural Coupling, *J. of Aircraft*, **43** (3), 2006.

[10] K.-J. Schultz, W. Splettstoesser, B. Junker, W. Wagner, E. Schoell, G. Arnaud, E. Mercker, K. Pengel, D. Fertis, A parametric wind tunnel test on rotorcraft aerodynamics and aeroacoustics (HELISHAPE) – Test Documentation and Representative results, DLR-IB-129-96/25, July 1996.

[11] R. Steijl, G.N. Barakos, and K.J. Badcock, Computational study of the advancing-side lift-phase problem, *J. of Aircraft*, **45 (1)**, 246-257, 2008.

[12] J.J.W. van der Vegt and H. van der Ven, Space-time discontinuous Galerkin finite element method with dynamic grid motion for inviscid compressible flows. Part I. General formulation. *J. of Comp. Physics*, **182**, 546-585, 2002.

[13] H. van der Ven and O.J. Boelens. Towards affordable CFD simulations of rotor in forward flight – a feasibility study with future application to vibrational analysis. In *proceedings of the 59th American Helicopter Society Forum, Phoenix, Arizona, USA, May 6-8, 2003*, 2003.

[14] H. van der Ven and O.J. Boelens. A framework for aeroelastic simulations of trimmed rotor systems in forward flight. In *proceedings of the 30th European Rotorcraft* F*orum, Marseille, September 14-16, 2004*, 2004.

[15] H. van der Ven, An adaptive multitime multigrid algorithm for time-periodic flow simulations, *J. of Comp. Physics*, **227**, 5286-5303, 2008.

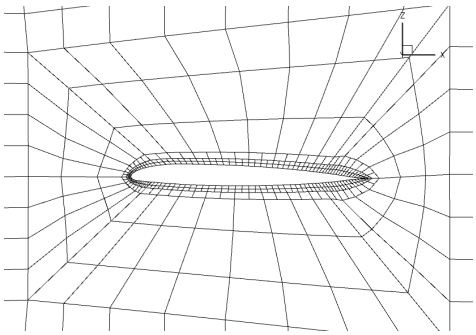

Figure 1 Blade cross section of the mesh after geometry refinement

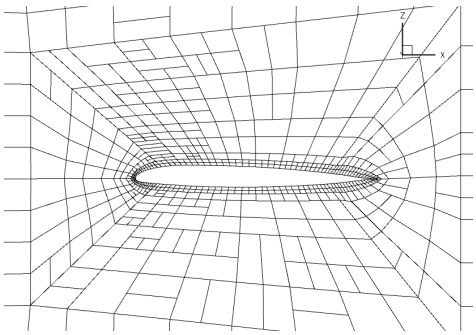

Figure 2 Same cross section after feature refinement

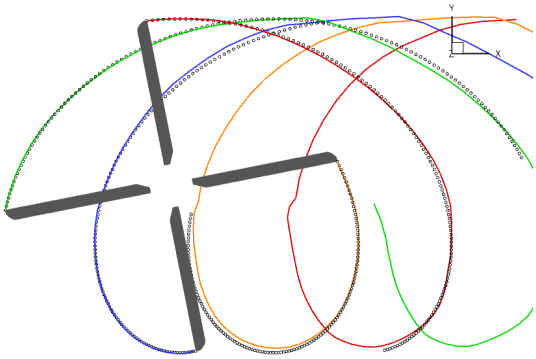

Figure 3 Difference between the blade tip trajectories and the predicted vortex locations using particle traces. Perpendicular view.

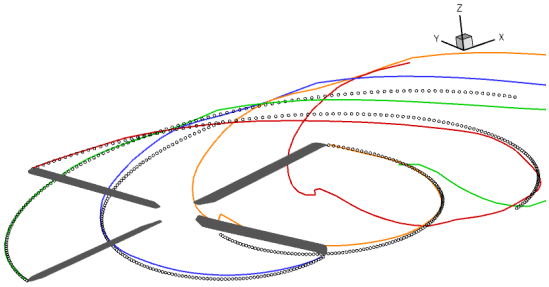

Figure 4 Difference between the blade tip trajectories and the predicted vortex locations using particle traces. Main difference is the effect of the downwash of the rotor.

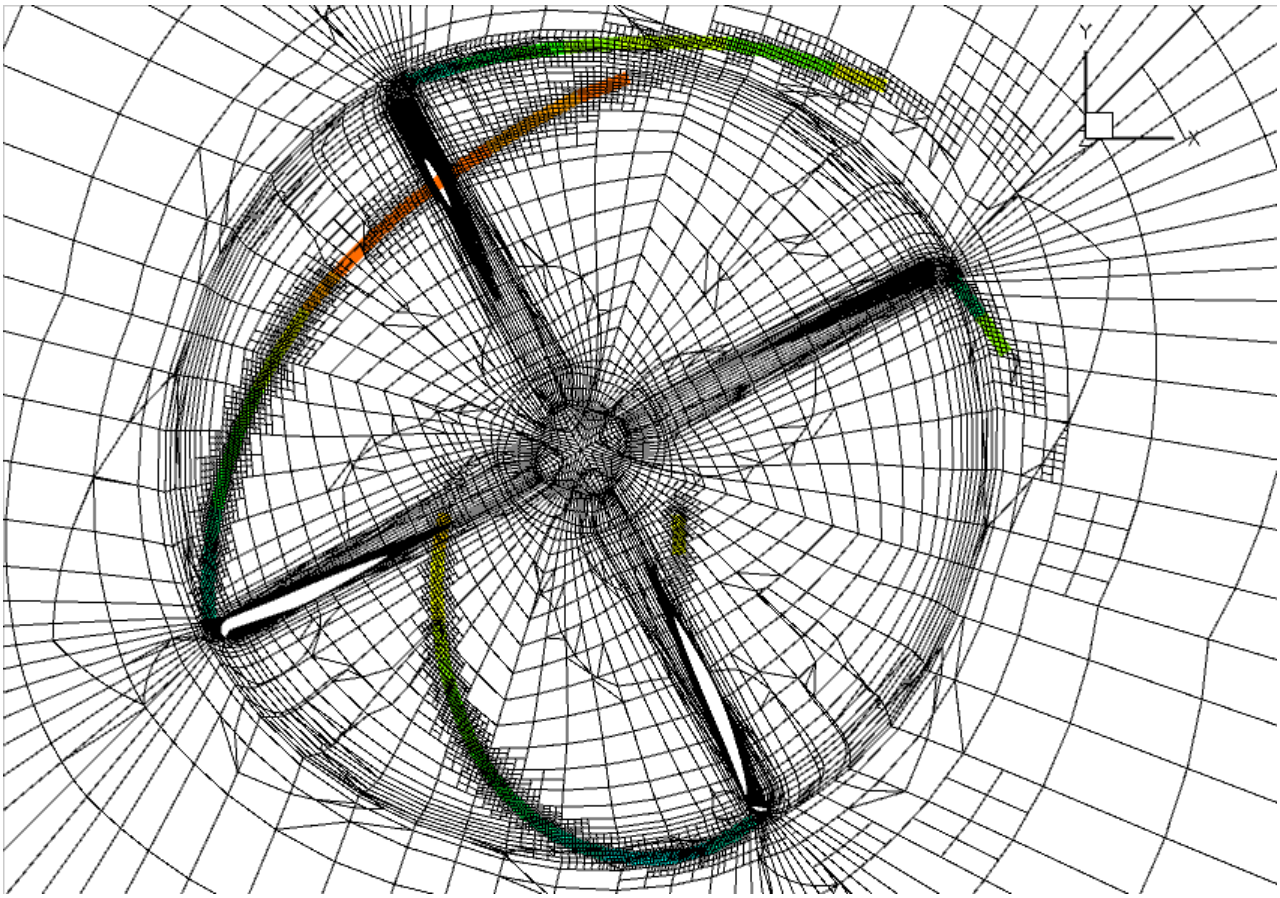

Figure 5 Illustration of the pre-adaptation strategy. An arbitrary horizontal slice of Mesh G3 is shown, together with the expected vortex locations as predicted by the particle traces. The vortex locations are coloured with their distance to plane, and not shown if the distance is greater than 0.0375R. Clearly visible is the refinement regions near the expected vortex locations.

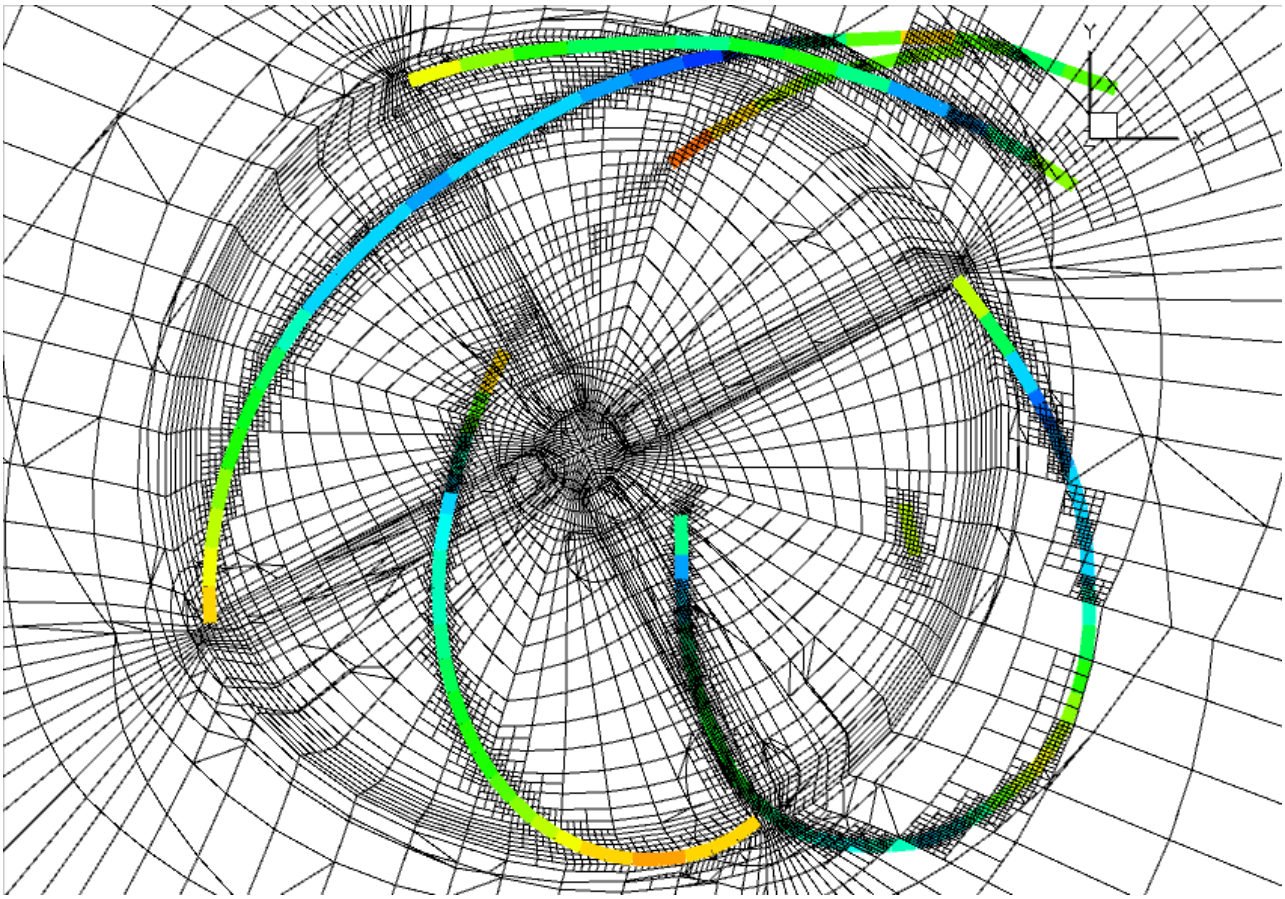

Figure 6 As the previous figure, but a different horizontal plane, below the previous one.

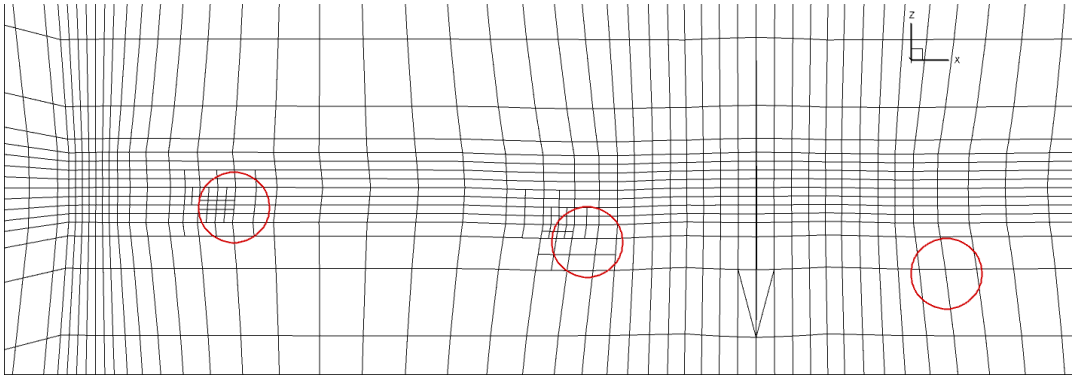

Figure 7 Impression of the mesh obtained from pre-adaptation on blade tip trajectories. The circles have a diameter of 0.1R.

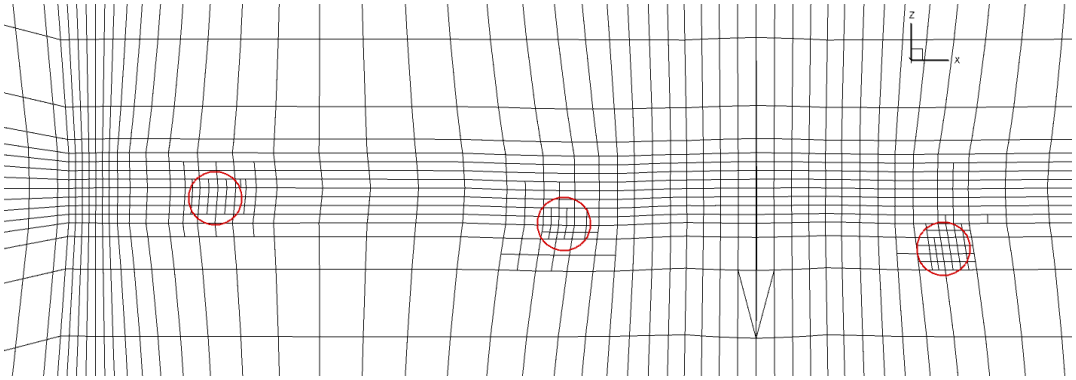

Figure 8 Impression of the mesh obtained from pre-adaptation on streak lines (target mesh width 0.0075R, attained mesh width about 0.01R). The circles have a diameter of 0.075R.

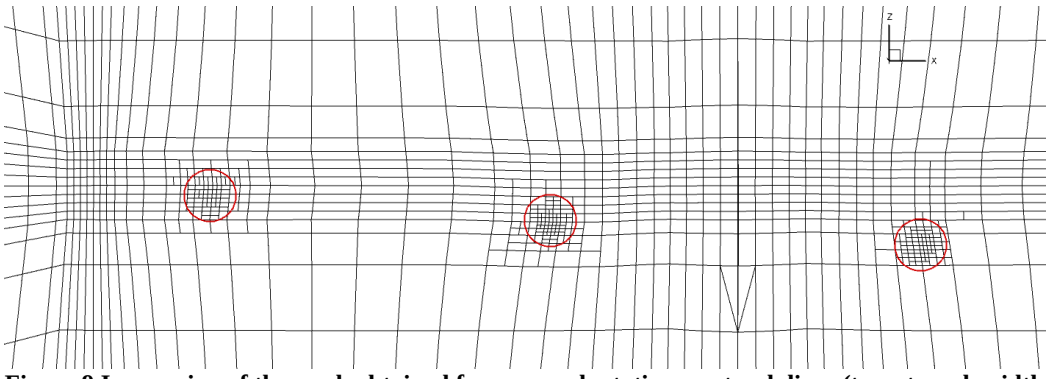

Figure 9 Impression of the mesh obtained from pre-adaptation on streak lines (target mesh width 0.005R, attained mesh width about 0.006R). The circles have a diameter of 0.075R.

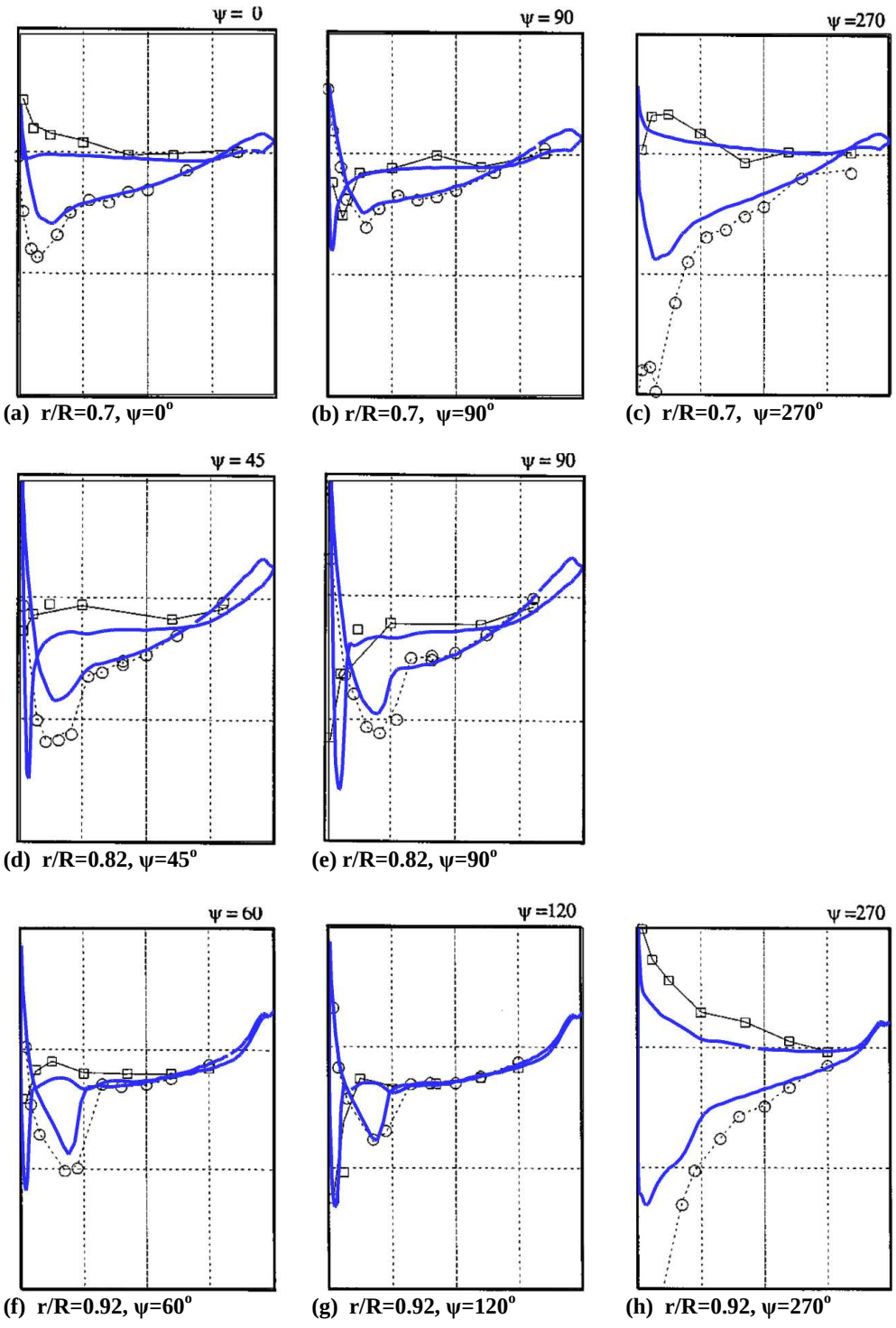

Figure 10 Pressure distributions at various span stations and azimuth angles. Dotted line with circles: experiment. Solid blue line: simulation. Shown is the pressure against chordwise position. Simulation on Mesh G3.

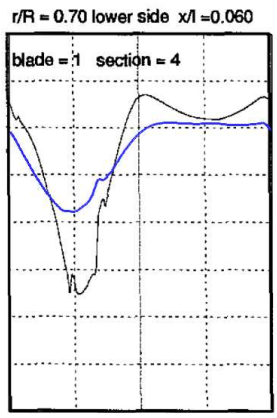

(a) r=0.7R, x/c=0.06 at lower side

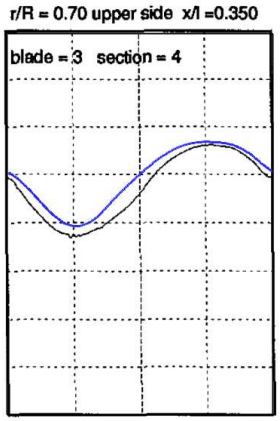

(b) r=0.7R, x/c=0.35 at upper side

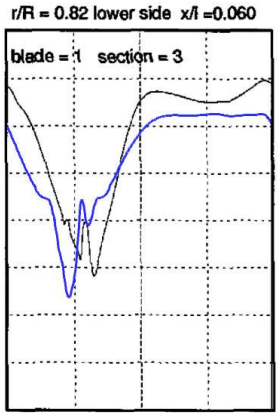

(c) r=0.82R, x/c=0.06 at lower side

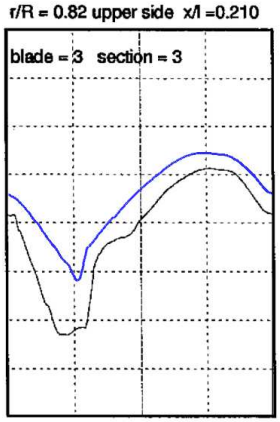

(d) r=0.82R, x/c=0.21 at upper side

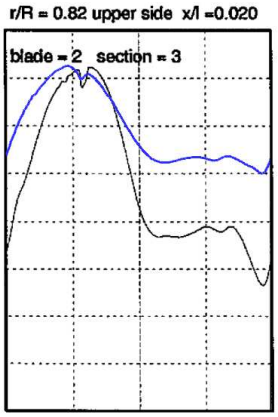

(e) r=0.82R, x/c=0.02 at upper side

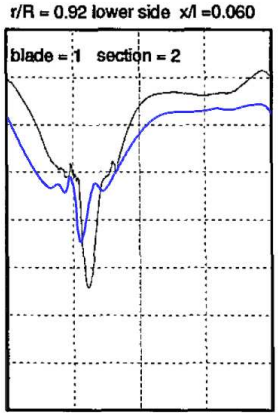

(f) r=0.92R, x/c=0.06 at lower side

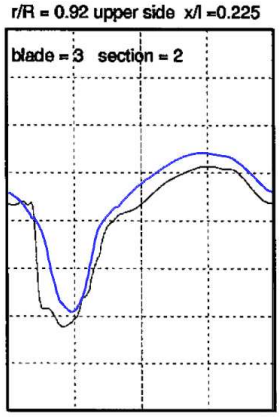

(g) r=0.92R, x/c=0.225 at upper side

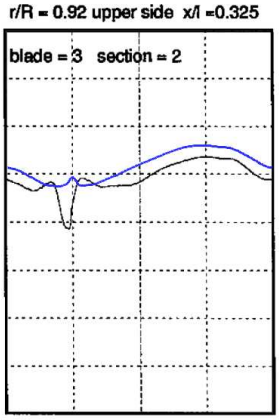

(h) r=0.92R, x/c=0.325 at upper side

Figure 11 Pressure histories at selected stations on the blade. Solid black line: experiment. Solid blue line: simulation. Shown is the pressure against azimuth angle for one revolution. Simulation on Mesh G3.

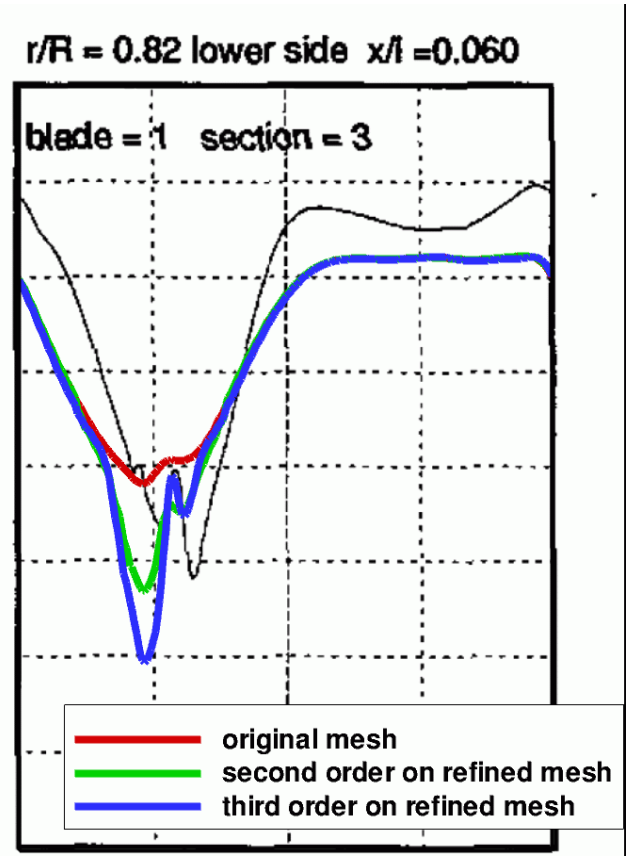

Figure 12 Comparison of time series of pressure at r/R=0.82 span station and x/c=0.06 chord station at the lower side. Red: Mesh G0, second order DG; Green: Mesh G2; second order DG; Blue: Mesh G2, third order DG.

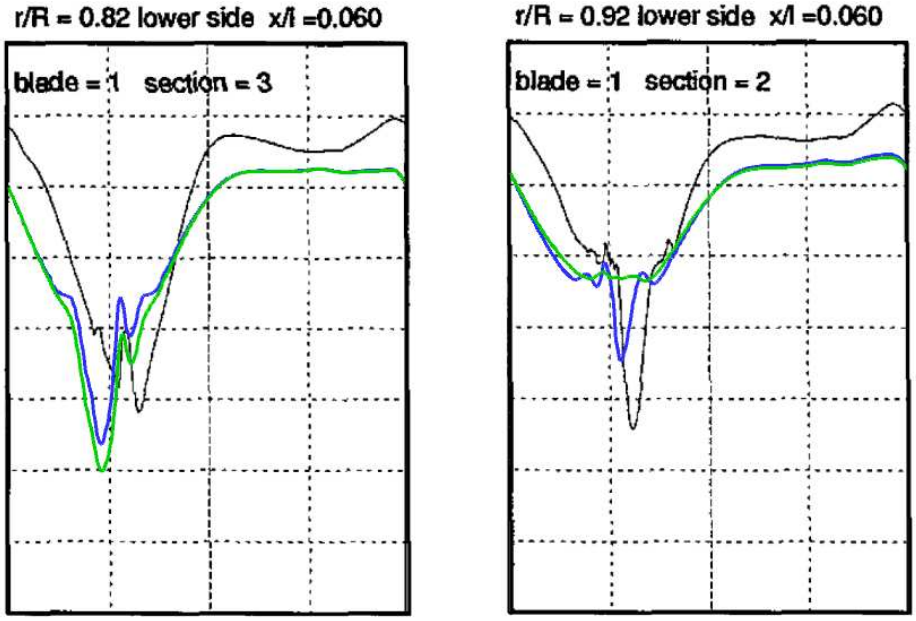

Figure 13 Comparison of pressure histories at selected stations. Solid black line: experiment. Solid green line: Mesh G2. Solid blue line: Mesh G3

(a) second order, Mesh G2

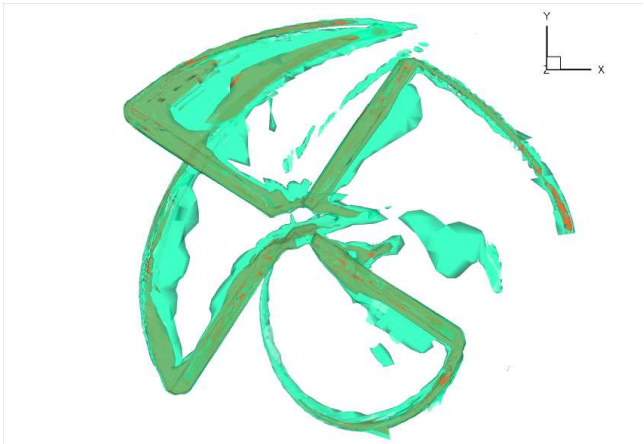

(b) third order, Mesh G2

(c) second order Mesh G3

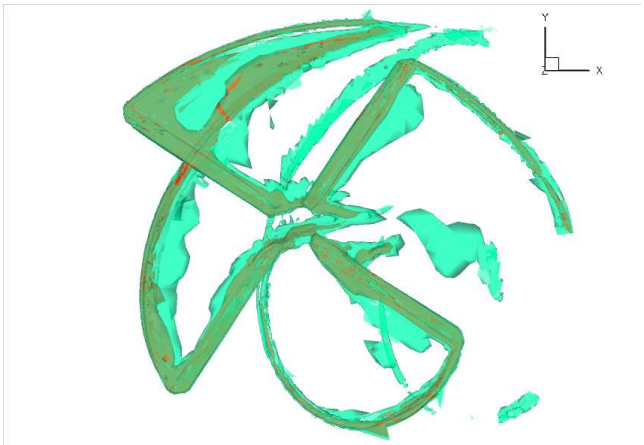

(d) third order, Mesh G3

Figure 14 Vorticity contours at azimuth angle of 56 degrees. Comparison between order of accuracy and mesh resolution. Iso-contours are shown at vorticity magnitude level of $2a_\infty/R$ and a_∞/R, where a_∞ is the speed of sound.

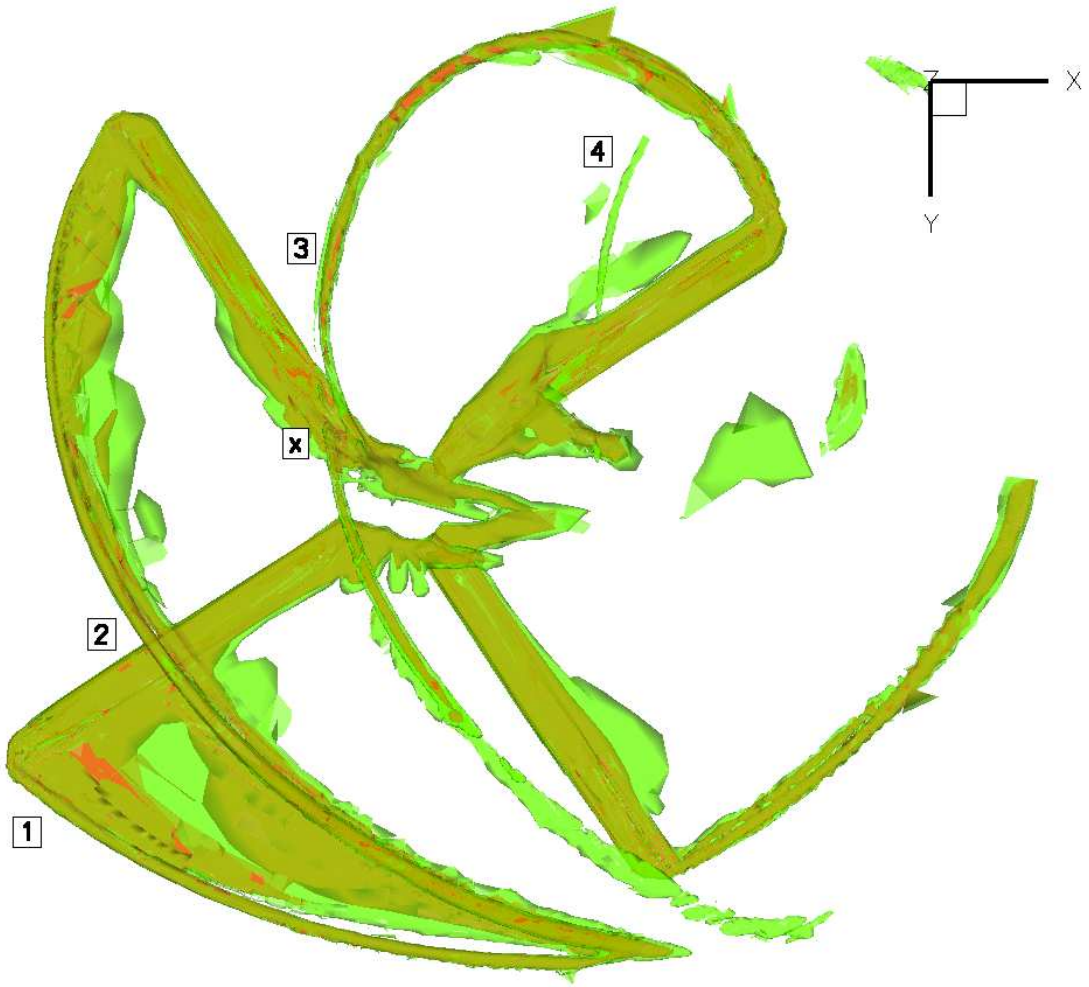

Figure 15 The vortex system at ψ=56°, as obtained on Mesh G3, viewed from below. Iso-contours are shown at vorticity magnitude level of $1.75a_\infty/R$ and $1.25a_\infty/R$, where a_∞ is the speed of sound.

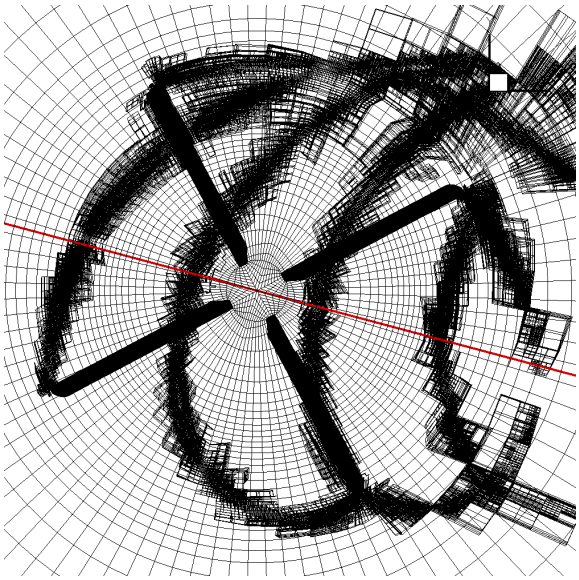

Figure 16 Definition of cross-section slice, shown in red, at ψ=28°, within Mesh G3.

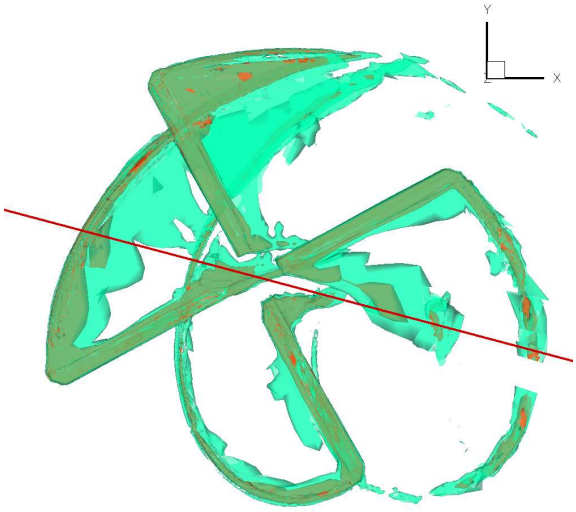

Figure 17 Vortex system at ψ=28°, as obtained on Mesh G3.

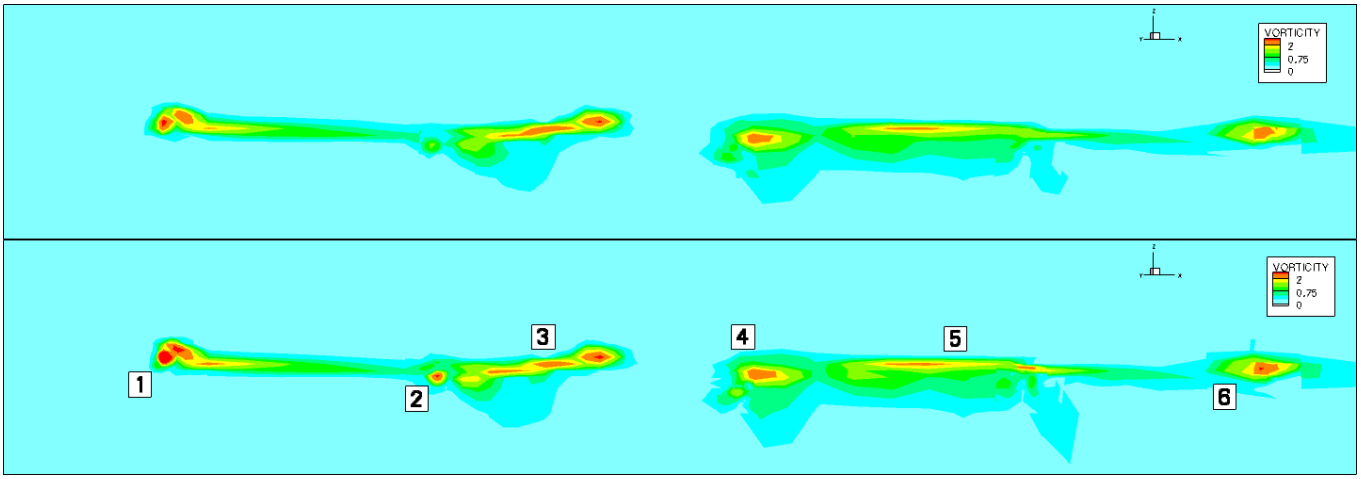

Figure 18 Comparison of vortex resolution in the slice defined in Figure 16 on Mesh G2 (top) and G3 (bottom)

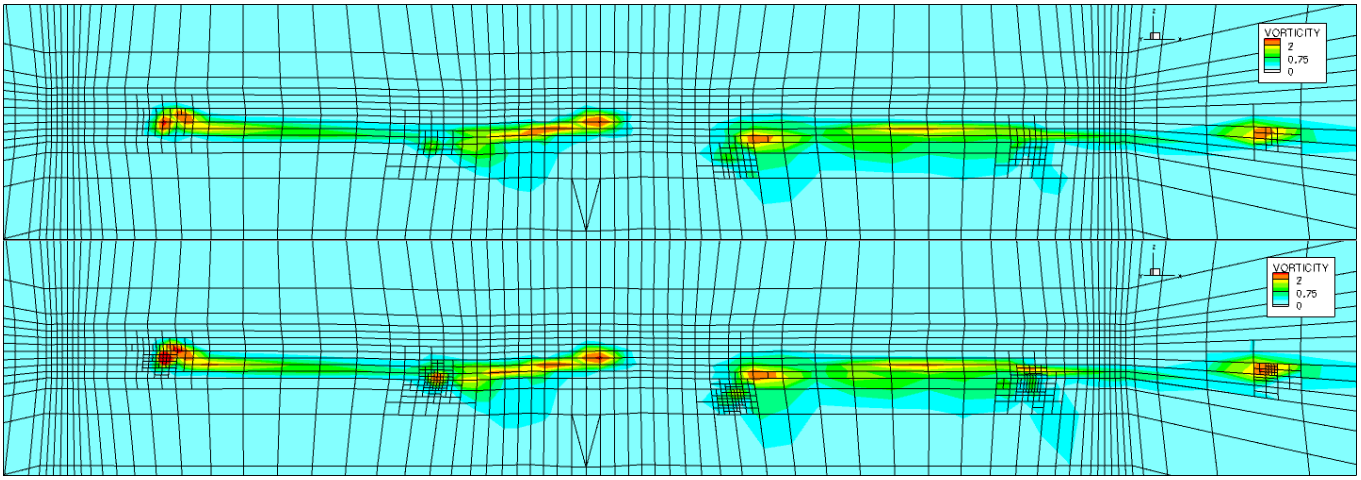

Figure 19 Comparison of vortex location and mesh refinement regions in the slice defined in Figure 16 on Mesh G2 (top) and G3 (bottom)

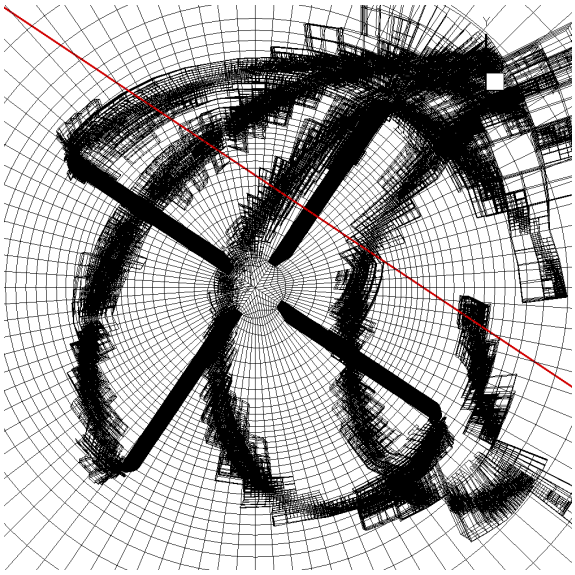

Figure 20 Definition of cross-section slice, shown in red, at ψ=56°, within Mesh G3.

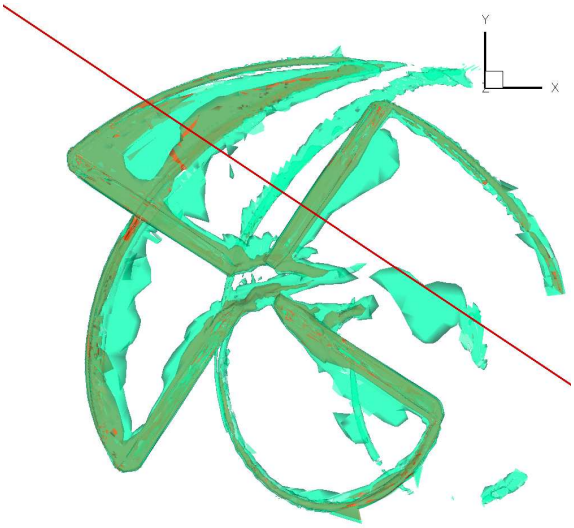

Figure 21 Vortex system at ψ=56°, as obtained on Mesh G3.

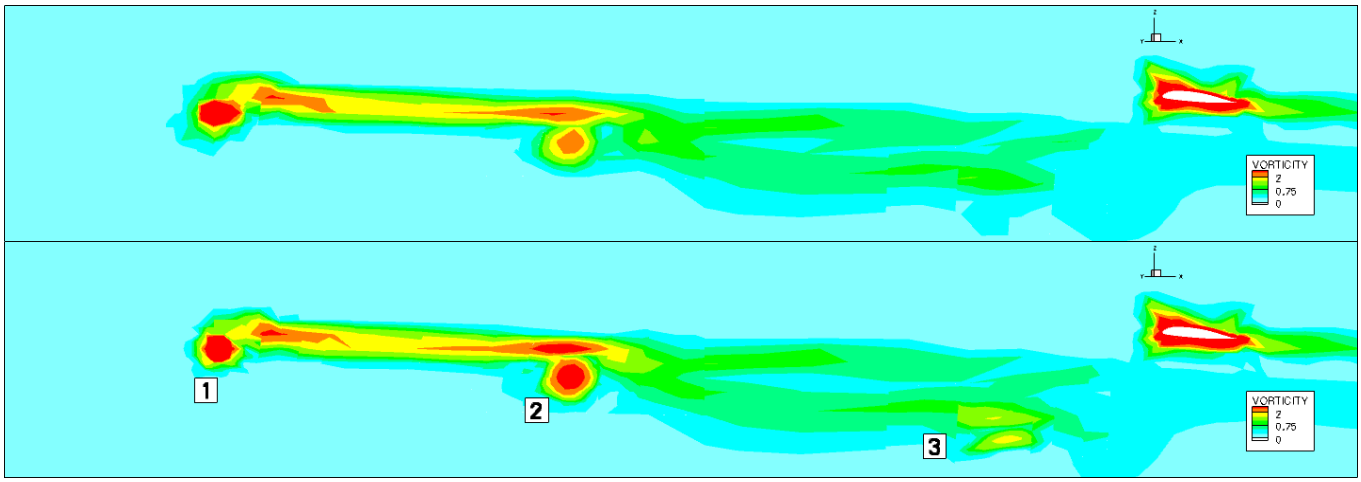

Figure 22 of vortex resolution in the slice defined in Figure 20 on Mesh G2 (top) and G3 (bottom).

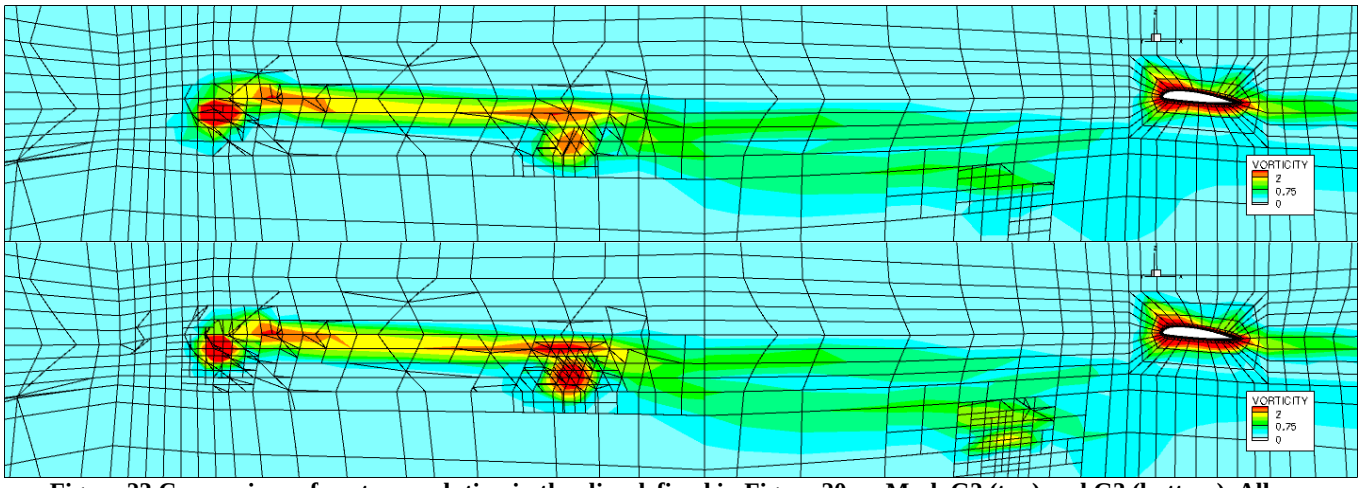

Figure 23 Comparison of vortex resolution in the slice defined in Figure 20 on Mesh G2 (top) and G3 (bottom). All cells are hexahedra, apparently triangular elements are a plotting anamoly.

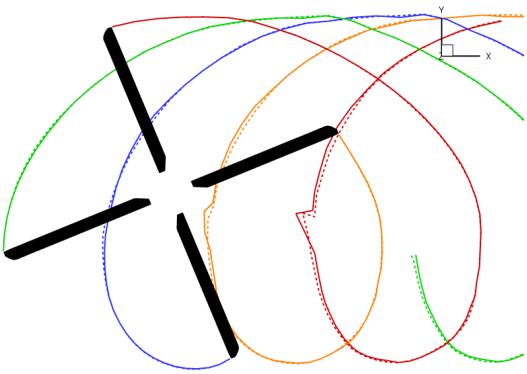

Figure 24 Comparison of streak lines. Solid: flow solution on Mesh G3, dashed: on Mesh G2

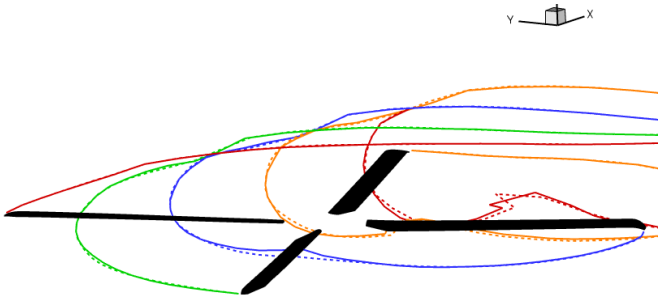

Figure 25 Comparison of streak lines. Solid: flow solution on Mesh G3, dashed: on Mesh G2

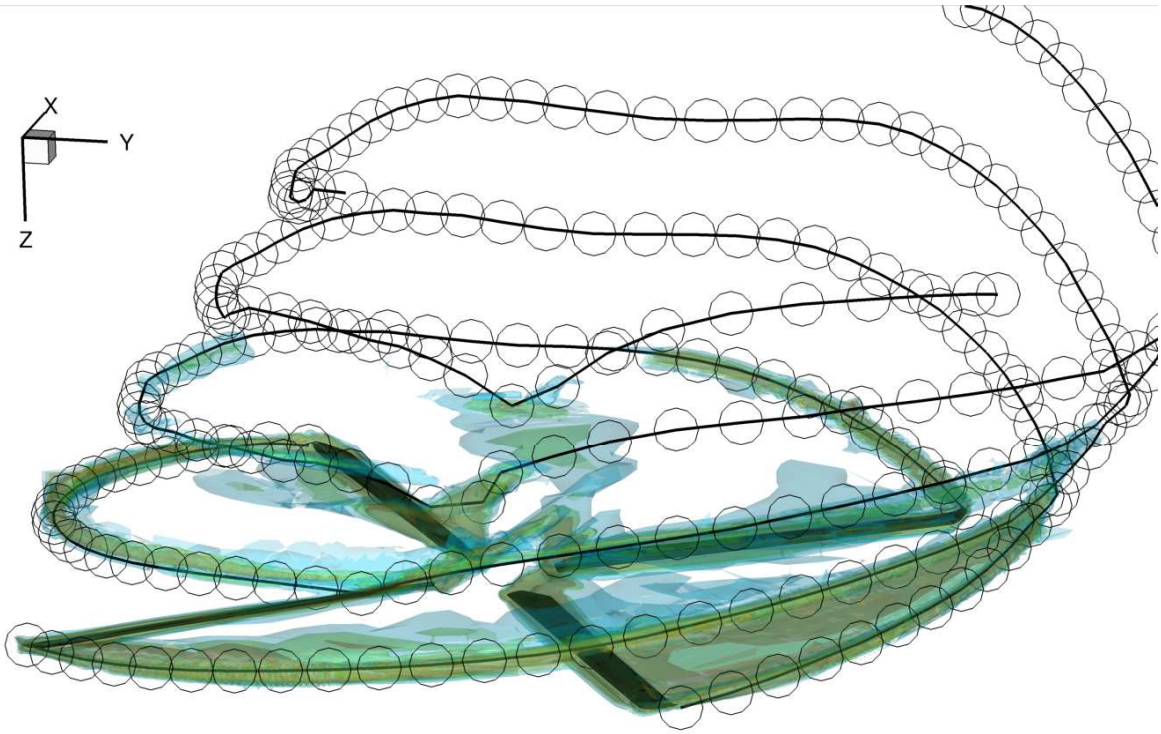

Figure 26 Comparison of tip vortex locations and streak lines of particles released at the blade tips. The circles have centres at the streak lines and radius equal to 0.0375*R*.